Whitlow W.L. Au
Arthur N. Popper
Richard R. Fay
Editors

Hearing by Whales and Dolphins

With 152 Illustrations

Springer

10
Acoustic Models of Sound Production and Propagation

JAMES L. AROYAN, MARK A. MCDONALD, SPAIN C. WEBB, JOHN A. HILDEBRAND, DAVID CLARK, JEFFREY T. LAITMAN, and JOY S. REIDENBERG

1. Introduction

Acoustic models based on physics and mathematics may yield significant advances in the understanding of sound production, propagation, and interaction associated with whales and dolphins. Models can be used to estimate the limits of intensity and frequency that are physically possible given the anatomy of a species. Models can also tell us what kind of anatomical structures would be necessary in order to produce sound having specific characteristics. Models can be used to clarify what type of measurements should be performed to answer specific questions. Many areas of bioacoustics stand to benefit from simulation of sound propagation through biological tissues and the media surrounding them. However, accurate modeling of biological subjects with complex anatomical features is extremely challenging, and few modern studies exist of sound production and propagation in whales and dolphins.

In this chapter, we will consider two acoustic models, the first dealing with the propagation of echolocation signals through the head of a dolphin. This model combines a novel tissue modeling approach with techniques of numerical wave propagation to study the acoustic principles operating in the biosonar emission and reception processes. The second model deals with the production of low-frequency sounds by the blue whale, *Balaenoptera musculus*. The features of blue whale sounds are considered and a sound production mechanism is derived taking the structures of the whale's anatomy into account along with the physics of acoustics. The first model results from the research of Aroyan (1996) and the second model is the result of research by the remaining authors.

2. Three-Dimensional Numerical Simulation of Biosonar Emission in the Common Dolphin

Measurements of the acoustic field of echolocating dolphins have demonstrated that dolphins emit a rapid series of intense pulses in a narrowly focused beam that emanates from the forehead and rostrum. Despite application of a variety of experimental techniques, the exact mechanisms involved in the generation, emission, and reception of delphinid biosonar signals have remained conjectural. Advances in the methodology of bioacoustic simulations have led to powerful combinations of techniques capable of addressing questions that have proven difficult to resolve experimentally. Aroyan (1996) combined methods for three-dimensional (3-D) acoustic simulation and far-field extrapolation with a novel approach to the mapping of acoustic tissue parameters from X-ray computed tomographic (CT) data. These techniques, applied to models of the forehead and lower jaw tissues of the common dolphin, *Delphinus delphis*, enabled a detailed study of the patterns of sound propagation within the modeled tissues and, hence, of the acoustic principles operating in the biosonar emission and reception processes. The following sections discuss the methods used in this investigation and present a series of results concerning the location of the biosonar signal source tissues, the roles of the skull, air sacs, and soft tissues (including the melon) in beam formation, and the acoustical consequences of forehead asymmetry in *Delphinus delphis*.

2.1 Computational Methods

The following approach was used to investigate the *D. delphis* emission system. First, computer models of the tissues of the dolphin's head were constructed using a novel mapping of both tissue density and acoustic velocity from X-ray CT attenuation data to a simulation grid. Second, 3-D finite difference programs were used to simulate acoustic propagation into the tissue models to locate the source region of the dolphin's biosonar emissions (analogous to the use of inverse seismologic simulations to pinpoint the underground source point or "hypocenter" of an earthquake, or to reversing the emission/collection role of an optical lens system). Third, sources were placed at these inverse simulation "hypocenters" or at conjectured anatomical source locations, and finite difference programs were again used to propagate the acoustic field of the source and tissue models out to a surface surrounding the tissue region of the grid. Fourth, boundary extrapolation programs were used to compute the emitted acoustic far-field from the pressure and its normal derivative over this surface. Biosonar mechanisms were investigated by visualizing the acoustic energy density within a variety of tissue models and by comparing the fields emitted by these models to the experimentally measured sonar emissions of live animals. Conceptually, this approach involves: (1) contructing the best pos-

sible acoustical model of the dolphin's tissues from the available data; (2) utilizing the reversibility of wave propagation to let the model tell us what its focal characteristics are; and (3) applying the resulting focal information in forward simulations to determine the emission properties for each model. Each step of this procedure has yielded new insights into the acoustic mechanisms of delphinid biosonar.

In order to study the patterns of sound propagation within the forehead tissues, propagation through tissue models was simulated by numerical integration of the acoustic wave equation. Shear wave velocities for soft tissues remain less than 1% of the compressional wave sound speed for frequencies below 1 MHz, and soft tissue shear wave attenuation coefficients are of the order of 10^4 times the compressional wave attenuation coefficients (Frizzell et al., 1976; Carstensen 1979; Madsen, et al., 1983). Additionally, the fact that air sacs normally cover much of the skull surface in the vicinity of the nasal passages in delphinids also suggests that shear modes do not play a significant role in biosonar emissions. In the current simulations, tissues (including bone) were modeled as inhomogeneous fluids and shear wave modes were ignored.

In fluids of inhomogeneous density and velocity, the linearized wave equation for acoustic pressure p is (Pierce 1981; Aroyan 1990):

$$\frac{1}{c^2(\mathbf{x})}\frac{\partial^2 p}{\partial t^2} = \nabla^2 p - \frac{\nabla p \cdot \nabla \rho(\mathbf{x})}{\rho(\mathbf{x})} \tag{1a}$$

Both the sound speed c and density ρ are functions of position $\mathbf{x}$, while the acoustic pressure p is dependent on position and time, $p = p(\mathbf{x}, t)$. By mapping the values of tissue velocity and density onto a grid, finite differencing schemes can be used to propagate the solution of Eq. 1a forward in time. The following discretization of Eq. 1a, solved for the numerical value of the acoustic pressure $P^{m+1}_{i,j,k}$ at grid position (i, j, k) and time step $(m + 1)$, was applied over the tissue region of the grid:

$$\begin{aligned}
P^{m+1}_{i,j,k} &= (2 - 7.5\kappa^2_{i,j,k})P^m_{i,j,k} - P^{m-1}_{i,j,k} \\
&+ \frac{4\kappa^2_{i,j,k}}{3}[P^m_{i+1,j,k} + P^m_{i-1,j,k} + P^m_{i,j+1,k} + P^m_{i,j-1,k} + P^m_{i,j,k+1} + P^m_{i,j,k-1}] \\
&- \frac{\kappa^2_{i,j,k}}{12}[P^m_{i+2,j,k} + P^m_{i-2,j,k} + P^m_{i,j+2,k} + P^m_{i,j-2,k} + P^m_{i,j,k+2} + P^m_{i,j,k-2}] \\
&- \frac{\kappa^2_{i,j,k}}{3\rho_{i,j,k}}[(P^m_{i+1,j,k} - P^m_{i-1,j,k}) - (P^m_{i+2,j,k} + P^m_{i-2,j,k})/8](\rho_{i+1,j,k} - \rho_{i-1,j,k}) \\
&- \frac{\kappa^2_{i,j,k}}{3\rho_{i,j,k}}[(P^m_{i,j+1,k} - P^m_{i,j-1,k}) - (P^m_{i,j+2,k} + P^m_{i,j-2,k})/8](\rho_{i,j+1,k} - \rho_{i,j-1,k}) \\
&- \frac{\kappa^2_{i,j,k}}{3\rho_{i,j,k}}[(P^m_{i,j,k+1} - P^m_{i,j,k-1}) - (P^m_{i,j,k+2} + P^m_{i,j,k-2})/8](\rho_{i,j,k+1} - \rho_{i,j,k-1})
\end{aligned} \tag{1b}$$

In this equation, $\kappa_{i,j,k} = (l/h)c_{i,j,k}$ is a nondimensionalized version of the spatially varying acoustic velocity $c_{i,j,k}$; $\rho_{i,j,k}$ is the spatially varying density; and $l = \Delta t$ and $h = \Delta x = \Delta y = \Delta z$ are the temporal and spatial grid increments, respectively. This scheme is fourth order in the spatial derivatives of pressure, second order in the spatial derivatives of density, and second order in the time derivative of pressure. The first three lines of Eq. 1b constitute the scheme for the homogeneous wave equation. This homogeneous scheme was used outside the tissue regions of the grid and greater than two points away from the grid edges. A second order spatial derivative scheme was applied at the next-to-last grid points. Absorbing boundary conditions were applied at the extreme grid edges to reduce reflections from grid boundaries to very low levels.

Figure 10.1a illustrates a typical simulation grid layout. The region of the grid containing the tissue model is indicated. Except for a few trials on half-resolution grids, a 1.5-mm cubic grid corresponding to the finest X-ray CT data voxel size was used in the forehead simulations. For the inverse simulations, the front face of the grid was used as a flat source to ensonify the tissue model region with a cosine-windowed "echo" at a fixed frequency and angle of return. A windowed aperture function was used to reduce the near-field diffraction of this source. The energy density at the focal maxima found in the inverse simulations were two to three orders of magnitude above variations caused by near-field diffraction and uneven ensonification of the model region.

Several different quantities may be calculated from the simulated pressure field and visualized with graphics packages in order to illustrate the patterns of sound propagation within the tissue models. For example, one may visualize the time-averaged magnitude of the total acoustic energy density W_{total} as the sum of the potential acoustic energy density $W_{\text{potential}}$ and the kinetic acoustic energy density W_{kinetic} (Pierce 1981; Morse and Ingard 1968)

$$W_{total} = W_{potential} + W_{kinetic} = \frac{1}{2\rho c^2}[\mathrm{Re}(p)]^2 + \frac{\rho}{2}|\mathrm{Re}(\mathbf{u})|^2 \qquad (2)$$

where the vector fluid velocity $\mathbf{u} = \nabla p/(i\omega\rho)$. Alternatively, one may visualize the time-averaged magnitude of the potential energy density $W_{\text{potential}} = [\mathrm{Re}(p)]^2/(2\rho c^2)$, as in Aroyan (1996). In this chapter, we will visualize either the total or the potential acoustic energy density, although all three forms of energy density (potential, kinetic, or total) and/or the acoustic intensity vector yield significant information regarding propagation within tissues.

In order to compute the emitted far-field patterns of various source and tissue models, the simulated pressure field and its normal derivative over a rectangular surface immediately surrounding the tissue region of the grid was used as input to boundary integral extrapolation programs. The

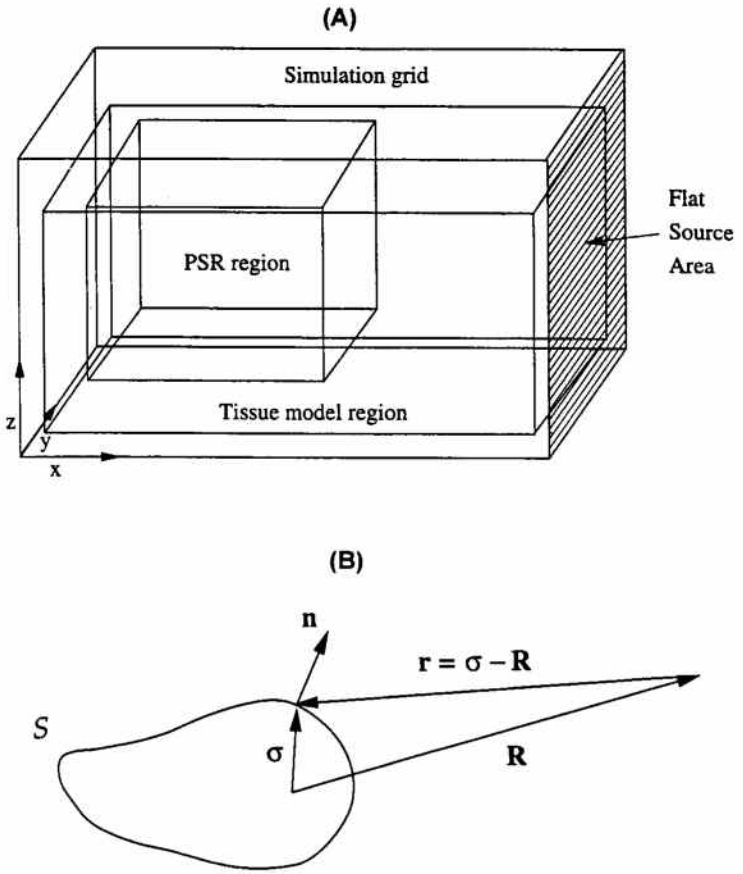

FIGURE 10.1. (A) Typical simulation grid layout. All inverse simulations used the front face of the grid as a flat source to ensonify the tissue region with "echoes" at various angles of return. In the inverse forehead simulations, the acoustic energy density within the subvolume labeled "PSR" was visualized. In all forward simulations, the pressure and its normal derivative over a surface immediately surrounding the source and tissue model were used to compute the far-field emission patterns. (B) Diagram of the geometry assumed by Eq. 3. Field points **R** are assumed to lie in the sourceless and homogeneous region exterior to the extrapolation surface S, which encloses an arbitrary source volume.

Helmholtz integral equation relates the pressure p and the normal derivative of the pressure $\partial p/\partial n$ over a surface S surrounding an arbitrary distribution of sources to the pressure $p(\mathbf{R})$ produced by those sources at any field point **R** (Baker and Copson 1953; Copley 1968; Schenck 1968). The geometry assumed here is illustrated in Figure 10.1b. For

points **R** lying exterior to the source volume enclosed by surface S, the Helmholtz integral equation has the form (Junger and Feit 1986; Aroyan 1996)

$$p(\mathbf{R}) = -\oint_S \left\{ p(\boldsymbol{\sigma}) \frac{\partial G(\boldsymbol{\sigma},\mathbf{R})}{\partial n} - G(\boldsymbol{\sigma},\mathbf{R}) \frac{\partial p(\boldsymbol{\sigma})}{\partial n} \right\} dS(\boldsymbol{\sigma}) \tag{3}$$

Here $\boldsymbol{\sigma}$ defines the vector coordinates of surface S, while $\partial/\partial n = \mathbf{n} \cdot \nabla$ denotes the directional derivative along the outward pointing unit vector **n** normal to surface S. We have also used the notation $G(\boldsymbol{\sigma}, \mathbf{R})$ for the 3-D free-space Green's function,

$$G(\boldsymbol{\sigma},\mathbf{R}) = -\frac{e^{ik|\boldsymbol{\sigma}-\mathbf{R}|}}{4\pi|\boldsymbol{\sigma}-\mathbf{R}|} = -\frac{e^{ikr}}{4\pi r}, \quad \mathbf{r} = \boldsymbol{\sigma} - \mathbf{R}, \tag{4}$$

where $k = \omega/c$ is the acoustic wave number, ω is the angular frequency of the field, and c is the (constant) speed of sound propagation at surface S and in the medium external to S. No assumptions are made about the distribution of sound sources, speeds, or other properties of materials inside surface S—this source region may be arbitrarily complex. In addition, S may be any closed surface surrounding the source region. The medium external to S, however, is assumed to be infinite, homogeneous, and sourceless. Because the extrapolation surface S can be located immediately outside the tissue model region of the simulation grid, an enormous reduction of the grid size required for far-field calculation is realized. In the current bioacoustic application, a far-field form of Eq. 3 was utilized: Appendix A gives this far-field formulation and notes aspects of its numerical implementation. Appendix A also provides an example of a simple computed far-field pattern and introduces an efficient representation of this data over all emission directions, which is used in all emission diagrams of Section 3.

2.2 *Model of the Dolphin*

This section outlines a new approach to modeling the acoustic parameters of delphinid soft tissues from X-ray CT attenuation data. This method generates approximations of the 3-D density and velocity distributions within scanned delphinid tissues that agree well with reported measurements.

An X-ray CT scan of the head of a male (body length = 1.92 m) common dolphin, *D. delphis*, was provided by Dr. Ted W. Cranford (identified as speciment D4 in Cranford et al. 1996). The spacing of the scan planes in the original CT data set varied from 5.0 mm over the rostrum, to 1.5 mm over the narial region, to 3.0 mm over the posterior cranium. Individual scans consisted of 320 × 320 pixel transverse sectional images on a 1.5-mm square grid. For simulation purposes, the tissue region of the original data was linearly interpolated in the x-direction to planes uniformly spaced 1.5 mm apart. The resulting data set was then used either at full resolution